Proceedings of the Canadian Society for Mechanical Engineering International Congress
32nd Annual Conference of the Computational Fluid Dynamics Society of Canada
Canadian Society of Rheology Symposium
CSME/CFDSC/CSR 2025
May 25–28, 2025, Montréal, Québec, Canada

NUMBER

AI-driven prediction of central plug morphology in Poiseuille flow of Bingham fluids with superhydrophobic walls

Amir Joulaei[1], Hossein Rahmani[1], Seyed Mohammad Taghavi[1]*

[1]Department of Chemical Engineering, Université Laval, Québec, QC, Canada, G1V 0A6
*Seyed-Mohammad.Taghavi@gch.ulaval.ca

DATE

***Abstract*—*This study presents a machine learning-based framework for predicting the flow behavior and central plug morphology of a viscoplastic Poiseuille flow in channels with two superhydrophobic (SH) walls. Here, the lower wall has constant hydrophobicity and groove characteristics, and the upper wall features varying groove periodicity length, slip area fraction, and slip number. Numerical simulations, conducted using OpenFOAM with the Papanastasiou regularization for modelling the viscoplastic fluid, generated a comprehensive database encompassing key flow parameters, including the Bingham number. Four predictive models* i.e.*, Adaptive Neuro-Fuzzy Inference System (ANFIS), Extreme Learning Machine (ELM), Support Vector Machine (SVM), and Multiple Linear Regression (MLR), were used. To assess the accuracy of the models, statistical indices such as correlation coefficient (R), variance accounted for (VAF), root mean square error (RMSE), mean absolute error (MAE), and mean absolute relative error (MARE), were employed. ANFIS demonstrated the highest accuracy, while ELM provided competitive performance with significantly faster computation and simpler hyperparameter tuning. A sensitivity analysis conducted using ELM revealed that the accurate prediction of the normalized area of the center plug is primarily influenced by the groove periodicity length of the upper wall.*

***Keywords-component*—Viscoplastic; Superhydrophobic; AI-prediction**

I. *INTRODUCTION*

Bingham fluids, a famous class of non-Newtonian fluids, represent yield stress values and are modeled by the Bingham constitutuve equation. Yield stress fluids play an important role in a wide range of industrial and engineering fields [1]. Depending on the application, these fluids may encounter different surface types, such as hydrophobic, hydrophilic, or superhydrophobic (SH) surfaces. Among these, SH surfaces have received particular attention due to their ability to minimize drag [2].

The flow of Newtonian fluids over SH surfaces has been extensively studied, with significant advancements reported in recent works [3]–[5]. However, investigations into the behavior of non-Newtonian fluids over SH surfaces remain relatively scarce [6]. Among the limited studies available, most have focused on shear-thinning fluids [7]. In recent years, attention has shifted toward the dynamics of viscoplastic fluids on SH surfaces. Semi-analytical and numerical analyses have been utilized to examine how channel thickness and groove orientation influence these flows. Research by Rahmani and Taghavi [8]–[12] showed that in thin channels, the unyielded central plug might deform significantly and even break under high slip conditions. In contrast, thick channels exhibit a relatively unaffected unyielded plug with a flat yield surface.

The use of two SH walls in channel flows has been extensively investigated, highlighting benefits such as improved drag reduction and enhanced effective slip lengths [13]. The configuration of the grooves on the opposing walls plays a key role, with distinct effects observed between aligned and misaligned grooves [13]. Specifically, misaligned grooves have been shown to be more effective in reducing pressure drop compared to their aligned counterparts [13]. In the context of viscoplastic flows, the effect of groove misalignment has also been studied [14], revealing that while the slip velocity is generally unaffected, the axial velocity profiles and the zones of the unyielded plug experience notable changes. Misaligned groove configurations, in particular, lead to significant alterations in the morphology of the central plug, resulting in pronounced yielding, deformation, and asymmetry.

The rapid progression of machine learning and artificial

Canada Research Chairs in Modeling Complex Flows

intelligence has opened new avenues for predicting the behavior of non-Newtonian fluids, utilizing their ability to model complex, nonlinear relationships. By employing extensive datasets, these machine learning models can effectively predict viscoplastic flow fields and yield surfaces, which are essential for understanding the behavior of such fluids [15]. In particular, deep learning architectures, such as convolutional neural networks (CNNs) and deep neural networks (DNNs), have gained prominence in addressing challenges in modeling non-Newtonian fluid dynamics. Mahmoudabadbozchelou *et al.* [16] proposed a multifidelity neural network (MFNN) approach, which integrates DNNs to estimate the rheological parameters of multicomponent complex fluids, improving the accuracy of rheological predictions. Furthermore, they introduced the Non-Newtonian Physics-Informed Neural Network (NN-PINN), a robust method for reconstructing velocity and pressure fields within a given domain, even under sparse or partially unknown boundary conditions [17]. More recently, Gao *et al.* [18] developed a Papanastasiou Regularization Physics-Informed Neural Network (PR-PINN) framework, applying it to the prediction and reconstruction of flow fields for Bingham fluids in isotropic circular and conical pipe geometries, further enhancing the understanding of flow behaviors in complex systems.

In this study, we advance the understanding of viscoplastic fluid flows over superhydrophobic surfaces by introducing a predictive framework based on artificial intelligence (AI). We employ four distinct AI models, *e.i.* Support Vector Machine (SVM), Linear Multiple Regression (LMR), Adaptive Neuro-Fuzzy Inference System (ANFIS), and Extreme Learning Machine (ELM), to predict the center unyielded plug area of Poiseuille viscoplastic flow, a key feature of viscoplastic flows. A comparative analysis of these methods is conducted to determine the most accurate and efficient model for predicting this key flow feature.

II. *Methodology*

A. *Flow configuration*

This study investigates the creeping Poiseuille flow of viscoplastic fluids in a planar channel with two transverse SH walls. The liquid-air interface is assumed to remain in a stable Cassie-Baxter state, which is valid at extremely low capillary numbers ($Ca \approx 10^{-5}$). Considering the practical difficulty of perfectly aligning the grooves on both walls, the study incorporates misalignment by introducing an offset parameter, $\varepsilon = \hat{\varepsilon}/\hat{L}_2$, where $\hat{\varepsilon}$ denotes the distance between the center of the grooves on the lower and upper SH walls. An offset value of $\varepsilon = 1/4$ is chosen, as it minimizes the pressure drop across the channel. The periodicity of the grooves on the lower and upper walls is represented by $\hat{L}_1$ and $\hat{L}_2$, respectively, and normalized with respect to the channel half-height $\hat{H}$, yielding the dimensionless periodicities $\ell_1 = \hat{L}_1/\hat{H}$ and $\ell_2 = \hat{L}_2/\hat{H}$. The analysis focuses on thin-channel configurations, where $\ell_1 = 7$ is fixed, and ℓ_2 varies within the range $0.2 \leq \ell_2 \leq 7$. For cases where $\ell_2 \leq 2$, configurations with multiple grooves on the upper wall are included in the investigation. The geometry of the grooves is defined by their width ($\hat{\delta}$), while the slip area fraction is expressed as $\varphi_{1,2} = \hat{\delta_{1,2}}/\hat{L}_{1,2}$.

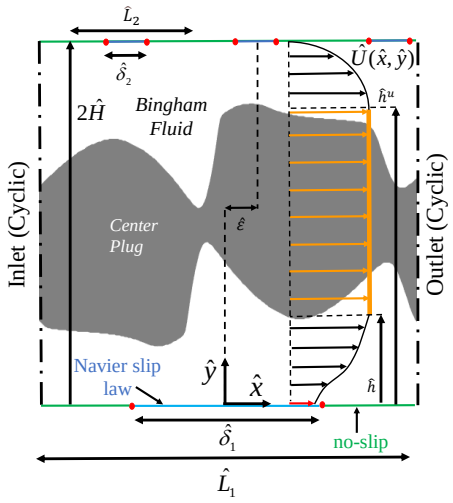

Figure. 1. Schematic illustration of plane Poiseuille-Bingham flow within a channel bounded by SH walls at the top and bottom. The SH walls are depicted with blue lines representing the flat liquid-air interfaces, which are modeled using the Navier slip condition, and green lines indicating the liquid-solid contact regions, where a no-slip condition is applied. The axial velocity profile is shown across the channel, with the central plug zone's velocity highlighted in orange. In the figure, dimensional flow parameters are denoted by a hat symbol ($\hat{\cdot}$), while dimensionless parameters are expressed without the hat.

The simulations are performed within a periodic computational domain containing a single groove on the lower SH wall, while the upper wall may feature one or multiple grooves depending on the value of ℓ_2. In this work, the geometry of the lower wall groove remains constant, resulting in fixed values for ℓ_1, φ_1, and b_1. Conversely, the morphology of the upper wall is varied, leading to changes in ℓ_2, φ_2, and b_2. The length of the periodic domain corresponds to the periodicity of the groove on the lower wall (see Fig. 1). Here, for $\ell_2 = 2$ and 5, we assumed that the upper wall pattern will be repeated along the channel to maintain the periodic flow. Thus, $\ell_2 = 2$ and 5 are the nominal periodicity lengths for the upper wall. Consequently, cyclic boundary conditions are applied at the inlet ($x = -\ell_1/2$) and outlet ($x = \ell_1/2$). Across all simulations, the channel half-height, the mean flow velocity, and the plastic viscosity are maintained constant under creeping flow conditions.

B. *Governing equations*

Here, the dimensionless form of the continuity and momentum conservation equations that govern the flow physics are expressed as:

$$\boldsymbol{\nabla}.\boldsymbol{U} = 0, \tag{1}$$

$$-\boldsymbol{\nabla}P + \boldsymbol{\nabla}.\boldsymbol{\tau} = 0, \tag{2}$$

where t is the time and $\boldsymbol{U} = Ue_x + Ve_y$ is the velocity vector (for the present two-dimensional flow). In addition, P

is the pressure, and $\boldsymbol{\tau}$ represents the deviatoric stress tensor. In order to reach the non-dimensional form of the momentum and continuity conservation equations, the characteristic velocity and stress are selected as the average velocity($\hat{U}_{ave}$) and viscous stress ($\hat{\mu}_p \frac{\hat{U}_{ave}}{\hat{H}}$), respectively, where the $\hat{\mu}_p$ is the plastic viscosity and $\hat{H}$ is chosen as the characteristic length.

The dimensionless form of the Bingham constitutive equation, which is used to model the viscoplastic rheology, is defined as:

$$\begin{cases} \boldsymbol{\tau} = \left(1 + \frac{B}{\dot{\gamma}}\right) \dot{\boldsymbol{\gamma}} & \tau > B, \\ \dot{\gamma} = 0 & \tau \leq B, \end{cases} \tag{3}$$

where $\boldsymbol{\tau}$ demonstrates the stress tensor, τ_0 is the yield stress of the Bingham material, $\dot{\boldsymbol{\gamma}}$ is the strain rate tensor ($\dot{\boldsymbol{\gamma}} = \boldsymbol{\nabla}.\boldsymbol{U} + (\boldsymbol{\nabla}.\boldsymbol{U})^{\boldsymbol{T}}$). Furthermore, the magnitude (norm) of stress and strain rate tensors are defined by the second invariant of each tensor. The Bingham number is expressed by considering the ratio between the fluid yield stress and the characteristic viscous stress ($B = \frac{\hat{\tau}_0 \hat{H}}{\hat{\mu}_p \hat{U}_{ave}}$).

For our two-dimensional flow, the magnitude of the strain-stress tensor reduces to:

$$\dot{\gamma} = \sqrt{\left(\frac{\partial U}{\partial y} + \frac{\partial V}{\partial x}\right)^2 + 4\left(\frac{\partial U}{\partial x}\right)^2}, \tag{4}$$

C. Computational setting

The finite volume simulations are conducted in OpenFOAM using the `simpleFoam` solver for steady-state analysis. The pressure-velocity coupling is handled through the SIMPLE algorithm, and convergence is achieved when the velocity residuals fall below a threshold of 10^{-8}. A non-uniform structured mesh is generated using `blockMesh`, with a finer resolution near the SH walls to accurately capture velocity gradients, particularly around the edges of the grooves [9]. To ensure that the results are independent of the mesh resolution, a mesh refinement study was carried out in a previous investigation [14].

Additionally, the reliability of the numerical model and the `simpleFoam` solver was verified through a comparison with an earlier two-phase numerical study [19] in our previous work [14], where a comparison demonstrated excellent agreement in velocity profiles for a transverse configuration, confirming the accuracy of our approach.

The liquid-air interfaces are represented using a linear Navier slip condition, implemented based on the framework developed by Vasudevan for OpenFOAM 2.2.x [20]. The viscoplastic behavior of Bingham fluids is modeled using the Papanastasiou regularization method [21]. The selection of the Papanastasiou regularization parameter is critical to accurately describe the flow behavior near the yield surface. For the present simulations, an initial value of 1000 is employed over approximately 7×10^6 iterations to achieve convergence, after which the parameter is increased to 5000 to enhance the resolution of velocity profiles and the precise identification of yield surface locations.

D. Data set collection

Database preparation plays a pivotal role in achieving better training and prediction performance for machine learning models. The proposed numerical approach facilitates the development of predictive models which can accurately estimate the area of unyeilded region within the viscoplastic Poiseuille flow in a channel with two SH walls, where the upper and lower walls exhibit different groove characteristics. The required flow field database for viscoplastic Poiseuille flow is generated using the OpenFOAM simulation results, encompassing a wide range of parameter combinations that critically influence flow behavior. This allows the machine learning models to capture the intricate relationships between the parameters and the output quantitative parameter. In particular, the groove periodicity length (ℓ_2) is varied as 0.2, 2, 5, and 7; the slip area fraction (φ_2) takes values of 0.1, 0.3, 0.5, 0.7, and 0.9; the slip number (b_2) ranges from 0.005 to 0.035 in increments of 0.005; and the Bingham number (B) is set to 1, 5, 10, 20, 30, 40, and 50. The flow field database generated through these OpenFOAM simulations serves as the training and testing dataset for the machine learning models.

E. Extreme Learning Machine

The Extreme Learning Machine (ELM) is an efficient learning algorithm designed for single-hidden-layer feedforward networks (SLFNs). It is widely recognized for its fast training speed, strong generalization capability, and minimal number of training epochs, making it a preferred choice for various machine learning applications [22]. ELM supports multiple activation functions, such as sigmoidal, sine, radial basis functions, and hard-limiting functions, while utilizing linear activation functions for the output neurons [23]. The ELM architecture consists of three layers: input, hidden, and output. A key characteristic of ELM is the random initialization of the weights and biases in the hidden layer, which removes the need for iterative optimization. The output weights are determined analytically through the Moore-Penrose generalized inverse, allowing the model to efficiently map inputs to outputs [24]. This distinct approach enables ELM to achieve high computational efficiency and strong performance in tasks like classification and regression. Its ability to quickly train without relying on iterative processes further contributes to its widespread use in machine learning tasks. Here, we utilize the ELM configuration with 15 hidden neurons, 200 maximum iterations, and radial basis activation function provides an optimal balance between model complexity and predictive accuracy.

F. Multiple Linear Regression

Multiple Linear Regression (MLR) is a commonly utilized method of linear regression, employed to model the relationship between multiple independent variables ($X_1, X_2, \ldots, X_k$) and a dependent variable (Y) [25]. The core task in MLR involves fitting a linear model to the data points, typically using the least squares approach. This method adjusts the regression equation's parameters in such a way that the sum

of the squared differences between the observed data and the predicted values is minimized. The resulting regression model is expressed as:

$$Y = \beta_0 + \beta_1 \times X_1 + \beta_2 \times X_2 + \beta_3 \times X_3 + \beta_4 \times X_4 + \cdots + \beta_k \times X_k \tag{5}$$

G. Support Vector Machine

Support Vector Machine (SVM) is a supervised learning method utilized for both classification and regression tasks. Support Vector Classification (SVC) is employed to partition data into distinct categories, while Support Vector Regression (SVR) is used to predict continuous values by fitting a model. SVR models the relationship between input x and output y as $y = f(x)$, which can be expressed as:

$$f(x) = w^T \phi(x) + b \tag{6}$$

where w and b represent the weight vector and bias term, respectively, and $\phi(x)$ is a kernel function. The objective of the model is to find an optimal hyperplane by solving a constrained optimization problem through Quadratic Programming. For high-dimensional data, the problem is reformulated using the duality theorem and Lagrange minimization, with the parameters w and b determined by the Karush-Kuhn-Tucker conditions. The support vectors, which are associated with non-zero Lagrange multipliers, play a crucial role in defining the regression function. Kernel functions, such as linear, sigmoid, Laplacian, Gaussian, exponential, rational quadratic (RQ), and polynomial, are used to facilitate computations in higher-dimensional feature spaces. Essential SVR parameters, including the choice of kernel, regularization parameter C, kernel bandwidth σ, and the ϵ-tube size for the ϵ-insensitive loss function, need to be carefully optimized to ensure optimal model performance [26]. The SVM configuration implements the Gaussian kernel function with the following parameter settings: $C = 10$, $\epsilon = 0.1$, and $\sigma = 0.3$.

H. Adaptive Neuro-Fuzzy Inference System

Fuzzy logic, introduced by Lotfi Asgarzadeh in 1965, offers a conceptual framework for reasoning, decision-making, and handling uncertainty [27]. The Adaptive Neuro-Fuzzy Inference System (ANFIS), developed by Jang in 1993, integrates neural networks with fuzzy logic to model complex nonlinear relationships. The ANFIS structure consists of five distinct layers: In Layer 1, membership functions are applied to the input variables to determine the degree of membership. Layer 2 calculates the firing strength of each rule based on the input memberships. In Layer 3, the firing strengths are normalized. Layer 4 applies a linear function to compute the output of each rule. Finally, Layer 5 aggregates these outputs to generate the overall result. ANFIS employs a hybrid learning approach that adjusts both the membership function parameters and the linear coefficients, thereby optimizing the system to effectively model input-output relationships [27]. For the ANFIS setup, we employ the BP-LS (Backpropagation-Least Squares) learning algorithm, utilizing four membership functions. The recommended number of iterations is 1000, which yields promising results by effectively balancing training duration and prediction accuracy.

III. *Results*

The variations in the upper wall characteristics lead to diversity in the morphology of the center unyielded plug. To further investigate the impact of characteristics parameters of the upper SH wall, including b_2, φ_2, ℓ_2, and B on the morphology of the center unyielded plug, the border of the unyielded plug (i.e. the yield surfaces) is demonstrated in Fig. 2. As shown in Fig. 2a and c, an increase in b_2 and ℓ_2 at a fixed Bingham number leads to significant deformation of the center plug (for example around $x = 0$). Interestingly, the slip area fraction of the upper SH wall (φ_2) exhibits a non-monotonic effect on the morphology of the center plug, where the significant deformation is observed in $\varphi_2 = 0.5$ according to Fig. 2b. Moreover, increasing the fluid's yield stress from a low Bingham number $B = 1$ to $B = 10$ (moderate range) causes the center plug to break near the groove edges. With a further increase in the Bingham number, the center plug near $x = 0$ (in addition to near $x = -\ell_1/4$ and $\ell_1/4$) undergoes more pronounced deformation and ultimately breaks completely at $B = 50$ (Fig. 2d).

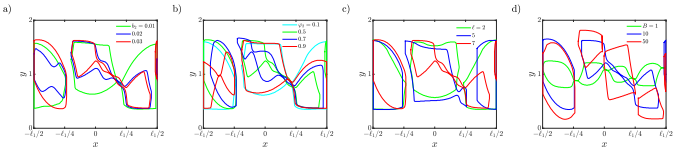

Figure. 2. The effect of upper wall's (a) slip number, (b) slip area fraction, (c) groove periodicity length, and (d) Bingham number on the morphology of the center unyielded plug obtained from the OpenFOAM results. In panels a-c, $B = 10$, while $\ell_2 = 7$ in panels a, b, and d. $\varphi_2 = 0.5$ in panels a, c, and d. Here, $b_2 = 0.03$ in panels b-d.

The influence of the upper SH wall's characteristics on the yielding behavior of the center plug can be quantified by calculating the total area of the unyielded zones, which is then normalized with respect to the corresponding plug area in the no-slip Poiseuille-Bingham flow (A/A_0). This normalized area of the center plug is used as an output for an AI-based prediction model. Four approaches, *i.e.* Multiple Linear Regression (MLR), Support Vector Machine (SVM), Extreme Learning Machine (ELM), and Adaptive Neuro-Fuzzy Inference System (ANFIS), are employed to predict the normalized area, as shown in Fig. 3(a–d), respectively. Here, the first row illustrates the training data, while the second row represents the test data. The vertical axis represents the predicted area through the AI model, while the horizontal axis shows the data obtained through the numerical simulations.

Each plot includes a diagonal line indicating perfect prediction, with 10% deviation bands around it to visualize the prediction accuracy. The data points within the 10% bands demonstrate good agreement between predictions and observations. As we move from MLR (Fig. 3a) to ANFIS (Fig. 3d), the distribution of data points becomes progressively closer to

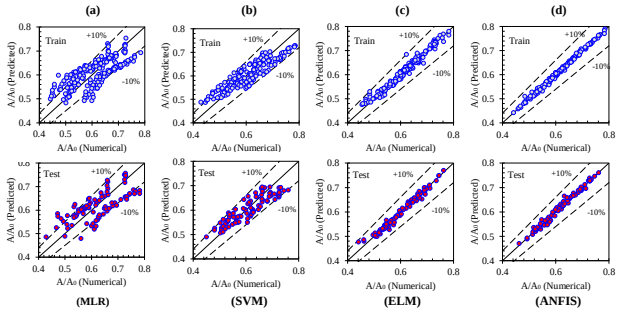

Figure. 3. Comparison of predicted and numerically simulated normalized plug areas using four AI-based prediction models: (a) Multiple Linear Regression (MLR), (b) Support Vector Machine (SVM), (c) Extreme Learning Machine (ELM), and (d) Adaptive Neuro-Fuzzy Inference System (ANFIS). The first row represents the training data, while the second row shows the test data. The vertical axis corresponds to the predicted normalized plug area from the AI models, and the horizontal axis represents the normalized plug area obtained through numerical simulations.

the perfect prediction line, indicating improved accuracy and better agreement between the predicted and observed values.

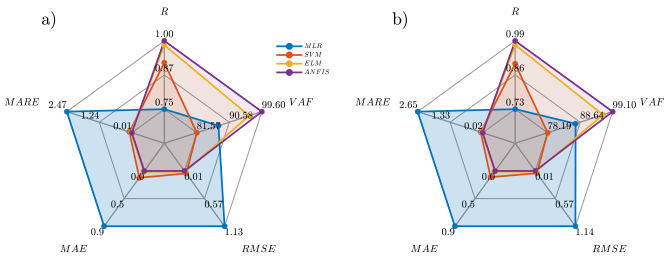

Figure. 4. The comparison of statistical indices (R, VAF, RMSE, MAE, and MARE) for different machine learning models: ANFIS, ELM, MLR, and SVM in (a) for the training data and (b) for the testing data.

Fig. 4 (a) for training and (b) for testing reveal the comparative performance of ANFIS, ELM, SVM, and MLR approaches across various statistical indices including Correlation Coefficient (R), Variance Accounted For (VAF), Root Mean Square Error (RMSE), Mean Absolute Error (MAE), and Mean Absolute Relative Error (MARE). ANFIS demonstrates superior performance, consistently achieving the highest scores in R (0.998 training, 0.995 testing) and VAF (99.6% training, 99.1% testing), while maintaining the lowest error rates (RMSE, MAE, MARE). ELM follows closely, showing strong correlation and accuracy, particularly in training ($R = 0.9805$ and VAF $= 96.1\%$). SVM exhibits moderate performance, outperforming MLR but falling short of ANFIS and ELM. MLR, while still providing useful results, shows the weakest performance among the four methods, with notably lower R and VAF values and higher error rates. The consistent pattern across both training and testing data suggests that ANFIS offers the most robust and accurate modeling approach for this particular dataset, with ELM as a strong alternative. In fact, it appears that ANFIS and ELM exhibit very similar performance in terms of evaluation metrics, with ANFIS performing slightly better than ELM. However, when factoring in time consumption, ELM stands out as a more efficient option, offering faster computations and ease of hyperparameter calibration.

Following the performance evaluation, a sensitivity analysis is conducted to examine the influence of different combinations of input parameters on the accuracy of the predicted normalized area of the center plug. Given the promising results obtained in the previous section, the ELM model is selected for this analysis. For the sensitivity study, we first consider a baseline model (Model 1), where all input parameters are included in the training process. Subsequently, in Models 2–5, only three out of the four input parameters are used to assess the relative importance of each parameter. By systematically varying the input parameter combinations (Table I), we aim to determine which parameter has the most significant impact on the model's predictive accuracy.

TABLE. I
COMBINATION OF SENSITIVITY ANALYSIS INPUT PARAMETERS VIA ELM-AI MODEL, WHERE ALL INPUT PARAMETERS ARE INCLUDED IN MODEL #1. FOR SUBSEQUENT MODELS, ℓ_2, φ_2, B, AND b_2 ARE EXCLUDED FOR MODELS #2, #3, #4, AND #5, RESPECTIVELY.

Model		ℓ_2	φ_2	B	b_2
Model #1	4 input	✓	✓	✓	✓
Model #2	3 input	×	✓	✓	✓
Model #3		✓	×	✓	✓
Model #4		✓	✓	×	✓
Model #5		✓	✓	✓	×

The trends observed in the R-values and performance metrics including VAF, RMSE, MAE, and MARE, as depicted in Fig. 5, demonstrate a clear dependency of the results on all geometrical parameters included in the analysis. However, among these parameters, the results exhibit a significantly stronger sensitivity to φ_2. This indicates that φ_2 has a more substantial impact on the model's performance metrics, with variations in this parameter leading to greater changes in the R-values, RMSE, and MAE, compared to the other geometrical parameters. Such a dependency underscores the critical role of φ_2 in influencing the accuracy and reliability of the sensitivity analysis outcomes.

IV. *Summary*

In this study, we investigated the effect of various parameters of the upper superhydrophobic (SH) wall on the morphology of the center unyielded plug and its subsequent behavior under different flow conditions. The results demonstrated that the characteristics of the upper SH wall, including slip number (b_2), slip area fraction (φ_2), groove periodicity length (ℓ_2), and Bingham number (B), have significant effects on the deformation and yielding behavior of the center plug. Specifically, an increase in b_2 and ℓ_2 at a fixed B led to a more

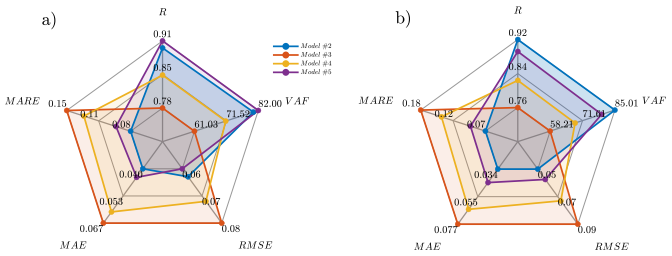

Figure. 5. The comparison of statistical indices (R, VAF, RMSE, MAE, and MARE) for evaluating the sensitivity analysis of different model based on Table. I in (a) for the training data and (b) for the testing data.

significant deformation of the center plug. Additionally, the slip area fraction (φ_2) exhibited a non-monotonic effect, with maximum deformation observed at $\varphi_2 = 0.5$. The increase in the Bingham number also influenced the breakage and deformation of the plug.

Furthermore, an AI-based prediction model was employed to quantify the effect of the upper SH wall's characteristics on the yielding behavior of the center plug. Four different machine learning models, *i.e.* Multiple Linear Regression (MLR), Support Vector Machine (SVM), Extreme Learning Machine (ELM), and Adaptive Neuro-Fuzzy Inference System (ANFIS), were used to predict the normalized area of the center unyielded plug. The comparison of the predicted and numerically simulated areas revealed that ANFIS outperformed the other models in terms of prediction accuracy, showing the highest correlation and lowest error rates. ELM also demonstrated strong performance, particularly in training, while SVM and MLR exhibited moderate performance, with MLR showing the weakest results.

ACKNOWLEDGMENT

This research was conducted at Université Laval with support from the Canada Research Chair in Modeling Complex Flows, the Canada Foundation for Innovation, and NSERC. AJ and HR acknowledge funding from ESSOR, Pierre-Viger, GPS, and CERMA PhD scholarships. We also appreciate the Digital Research Alliance of Canada for providing high-performance computing resources.

REFERENCES

[1] N. J. Balmforth, I. A. Frigaard, and G. Ovarlez, "Yielding to stress: recent developments in viscoplastic fluid mechanics," Annual review of fluid mechanics, vol. 46, pp. 121–146, 2014.

[2] Y. Xu, C. Ruan, and Z. Zhang, "Numerical Study on Drag Reduction of Superhydrophobic Surfaces with Conical Microstructures in Laminar Flow," vol. 17, pp. 1129–1142, 2024.

[3] H. Miyoshi, H. Rodriguez-Broadbent, A. Curran, and D. Crowdy, "Longitudinal flow in superhydrophobic channels with partially invaded grooves," Journal of Engineering Mathematics, vol. 137, p. 3, 2022.

[4] H. Rodriguez-Broadbent, H. Miyoshi, and D. G. Crowdy, "Asymptotically exact formulas for channel flows over liquid-infused surfaces," IMA Journal of Applied Mathematics, p. hxae026, 2024.

[5] S. Zimmermann and C. Schönecker, "Analytical models for pressure-driven Stokes flow through superhydrophobic and liquid-infused tubes and annular pipes," Journal of Fluid Mechanics, vol. 978, p. A20, 2024.

[6] H. Rahmani, F. Larachi, and S.M. Taghavi, "Modeling of shear flows over superhydrophobic surfaces: from Newtonian to non-Newtonian fluids," ACS Engineering Au, vol. 4, pp. 166–192, 2024.

[7] P. K. Ray, D. Bouvier, and D. T. Papageorgiou, "Flow of shear-thinning liquids in channels with superhydrophobic surfaces," Journal of Non-Newtonian Fluid Mechanics, vol. 319, p. 105091, 2023.

[8] H. Rahmani and S.M. Taghavi, "Poiseuille flow of a Bingham fluid in a channel with a superhydrophobic groovy wall,"Journal of Fluid Mechanics, vol. 948, p. A34, 2022.

[9] H. Rahmani and S. M. Taghavi, "Viscoplastic flows in thin superhydrophobic channels,"Journal of Non-Newtonian Fluid Mechanics, vol. 315, p. 105016, 2023.

[10] H. Rahmani, H. Kumar, J. Greener, and S. M. Taghavi, "Yield stress fluid flows in superhydrophobic channels: From creeping to inertial regime,"Physics of Fluids, vol. 35, 2023.

[11] H. Rahmani and S.M. Taghavi, "A comprehensive model for viscoplastic flows in channels with a patterned wall: longitudinal, transverse and oblique flows,"Journal of Fluid Mechanics, vol. 984, p. A32, 2024.

[12] H. Rahmani and S. M. Taghavi, "Viscoplastic flows in superhydrophobic channels with oriented grooves: From anisotropic slip to secondary flow,"Journal of Non-Newtonian Fluid Mechanics, vol. 326, p. 105203, 2023.

[13] A. Shadloo-Jahromi, M. Kharati-Koopaee, and O. Bavi, "Friction factor calculation in nanochannels comprising different wall hydrophobicities and superhydrophobic structures: Molecular dynamic simulations,"International Communications in Heat and Mass Transfer, vol. 117, p. 104763, 2020.

[14] A. Joulaei, H. Rahmani, and S. M. Taghavi, "Effects of wall groove misalignment on viscoplastic flow dynamics in superhydrophobic channels,"Physical Review Fluids, vol. 9, p. 123301, 2024.

[15] Y. Zhang, Z. Dong,M. S. Obaidat, and X. Ban, "Non-Newtonian fluid simulation and reconstruction from monocular videos,"Simulation Modelling Practice and Theory, vol. 123, p. 102688, 2023.

[16] M. Mahmoudabadbozchelou, M. Caggioni, S. Shahsavari, W. H. Hartt, G. Em Karniadakis, and S. Jamali, "Data-driven physics-informed constitutive metamodeling of complex fluids: A multifidelity neural network (MFNN) framework,"Journal of Rheology, vol. 65, pp. 179–198, 2021.

[17] M. Mahmoudabadbozchelou, G. E. Karniadakis, and S. Jamali, "nn-PINNs: Non-Newtonian physics-informed neural networks for complex fluid modeling,"Soft Matter, vol. 18, pp. 172–185, 2022.

[18] Z. Gao, R. Yin, R. Zhai,J. Lin, and D. Yin, "A deep learning framework for solving the prediction and reconstruction problem of Bingham fluid flow field,"Physics of Fluids, vol. 36, 2024.

[19] M. G. Arun, D. Dilip, and S. K. Ranjith, "Effect of interface curvature on isothermal heat transfer in a hydrophobic microchannel with transverse ribs and cavities,"International Journal of Thermal Sciences, vol. 167, p. 107014, 2021.

[20] M. Vasudevan, "Implementation of partially slip boundary conditions,"In Proceedings of CFD with OpenSource Software, 2017.

[21] T. C. Papanastasiou, "Flows of materials with yield,"Journal of Rheology, vol. 31, pp. 385–404, 1987.

[22] G. Huang, G. B. Huang, S. Song, and K. You, "Trends in extreme learning machines: A review,"Neural Networks, vol. 61, pp. 32–48, 2015.

[23] G. Huang, Q. Y. Zhu, and C. K. Siew, "Extreme learning machine: theory and applications,"Neurocomputing, vol. 70, pp. 489–501, 2006.

[24] J. Lu, W. Zeng, L. Zhang, and Y. Shi, "A novel key features screening method based on extreme learning machine for Alzheimer's disease study,"Frontiers in Aging Neuroscience, vol. 14, p. 888575, 2022.

[25] V. Sellam and E. Poovammal, "Prediction of crop yield using regression analysis,"Indian Journal of Science and Technology, vol. 9, pp. 1–5, 2016.

[26] Y. Rabbani, M. Shirvani, S. H. Hashemabadi, and M. Keshavarz, "Application of artificial neural networks and support vector regression modeling in prediction of magnetorheological fluid rheometery,"Colloids and Surfaces A: Physicochemical and Engineering Aspects, vol. 520, pp. 268–278, 2017.

[27] K. Roushangar, S. Akhgar, F. Salmasi, and J. Shiri, "Modeling energy dissipation over stepped spillways using machine learning approaches,"Journal of Hydrology, vol. 508, pp. 254–265, 2014.